Available online at www.sciencedirect.com

SCIENCE DIRECT®

ELSEVIER

Journal of Non-Crystalline Solids 352 (2006) 2801–2810

JOURNAL OF NON-CRYSTALLINE SOLIDS

www.elsevier.com/locate/jnoncrysol

γ-Fe_2O_3/SiO_2 nanocomposites for magneto-optical applications: Nanostructural and magnetic properties

D. Ortega [a,*], J.S. Garitaonandia [b], C. Barrera-Solano [a], M. Ramírez-del-Solar [a], E. Blanco [a], M. Domínguez [a]

[a] *Departamento de Física de la Materia Condensada, Facultad de Ciencias, Universidad de Cádiz, Campus Universitario del Río San Pedro, 11510 Puerto Real (Cádiz), Spain*

[b] *Departamento de Física Aplicada II, Facultad de Ciencias, Universidad del País Vasco,Apartado 644, 48080 (Bilbao), Spain*

Received 22 July 2005; received in revised form 3 March 2006

Available online 9 June 2006

Abstract

Monolithic nanocomposites consisting in γ-Fe_2O_3 (maghemite) nanoparticles embedded in a silica gel have been prepared as potential magneto-optic materials, suitable for magnetic field sensing. The effects of several processing parameters on the structural and magnetic properties of the samples were evaluated to optimize their performance. Their structural properties have been studied by means of X-ray diffraction, thermogravimetric analysis and transmission electron microscopy, while the magnetic behavior has been characterized by Mössbauer spectroscopy and Faraday magnetometry. Our results indicate that maghemite crystallization conditions must be carefully controlled to obtain nanoparticles of an adequate size and to avoid subsequent evolution to other undesired ferric oxide phases.

PACS: 81.20.Fw; 81.07.Bc; 81.40.Rs; 76.80.+y

Keywords: Magnetic properties; Mossbauer effect and spectroscopy; TEM; Nanocomposites; Nanoparticles; Sol–gels (xerogels); Thermal properties; X-ray diffraction

1. Introduction

The study of maghemite (γ-Fe_2O_3)/silica nanocomposites has been undertaken from several points of view, regarding either their synthetic route [1] or their final technological applications [2]. We have specifically focused our investigation on xerogels containing ferrimagnetic maghemite nanoparticles, not only for their optical [3,4], magnetic [5–8] and magneto-optic [9,10] properties, but also because of their particular structure, which acts like a modifier of the properties that the nanoparticles would have out of the gel matrix, either in a suspension or in a bulk form. Maghemite/silica composites, as previously reported by other authors [11,12], exhibit magneto-optical Faraday effect (MOFE), which is a desirable feature to develop magnetic field sensors from these materials [13,14].

Maghemite is a ferrimagnetic material which represents the low temperature phase of iron oxide, and it easily evolves into the more stable phase, hematite (α-Fe_2O_3), when submitted to high temperatures. Thus, special care must be taken to avoid the appearance of hematite while iron oxide xerogels are heat treated at temperatures above 500 °C, since its antiferromagnetic nature can seriously affect the desired ferrimagnetic behavior of the final nanocomposite. In addition, the silica matrix magnetic dilution effect, the superparamagnetic behavior of the smallest particles and the coexistence of more than one iron oxide phase give rise to a complex magnetic response. The present work is aimed to investigate the influence of processing conditions in the tailoring of magnetic properties of these

---

* Corresponding author. Tel.: +34 956 016 569; fax: +34 956 016 288. *E-mail address:* daniel.ortega@uca.es (D. Ortega).

0022-3093/$ - see front matter © 2006 Elsevier B.V. All rights reserved.
doi:10.1016/j.jnoncrysol.2006.03.056

kinds of systems. Results of the magneto-optical characterization of these samples will be published elsewhere [15].

2. Experimental

Iron oxide (γ-Fe_2O_3) particles hosted in a silica matrix have been synthesized by the sol–gel method. Tetraethoxysilane (TEOS) and $Fe(NO_3)_3 \cdot 9H_2O$ were used as precursors with a Fe/Si ratio of 15 wt%. Samples were prepared at room temperature following the classical method, by hydrolysis of TEOS (ethanol diluted at 30%) with 4 mol H_2O/mol TEOS, where the iron salt was previously dissolved. Aqueous salt solution pH was adjusted to the values indicated in Table 1 with nitric acid. The homogeneous solution was mechanically stirred for 5 min. Finally, formamide, used as a drying control chemical additive (DCCA), was added in a molar ratio of 4 mol/mol TEOS. The resulting sols were kept in hermetically sealed cylindrical tubes and left for gelation at a fixed temperature of 50 °C. In all samples, the gelation point was reached after 1 day approximately. To ensure complete removal of syneresis liquid, samples were aged during different periods of several days and dried at 50 °C for five days. During this stage, a progressive darkening of samples was observed, probably due to iron complexation as $Fe[(H_2O)_6]^{3+}$ [16] and subsequent evolution to fresh polymeric species as the sol pH value approaches 2.5 after the formamide addition, which is the maximum value measured value during the monitoring of gelation period [16,17].

Finally, the samples were heat treated up to 700 °C in a nitrogen stream (0.1 l/min), in order to eliminate the residuals from the pore network, promote the crystallization of γ-Fe_2O_3 particles and stabilize them.

Thermogravimetric analyses (TGA) of the samples were performed in a Perkin–Elmer TGA7 with constant heating rate experiments at 0.5 °C/min, in the 50–900 °C range, on monolithic pieces. Crystallization of the particles into the composites was studied by X-ray diffraction (XRD) in a PHILIPS PW1830 diffractometer using CuK_α radiation in the 10–90° angular range. The microstructure of the samples was observed by transmission electron microscopy (TEM) using a JEOL 1200-EX equipment. Magnetization measurements were performed by a commercial Faraday Balance (Oxford Instruments), as a function of applied magnetic field (0–0.6 T), at room temperature. ^{57}Fe Mössbauer spectra were collected at room temperature in the transmission geometry using a conventional constant-acceleration spectrometer with a ^{57}Co–Rh source.

3. Results

Table 1 shows the main processing parameters for a set of samples, varying synthesis pH medium and aging time while the rest of parameters remain essentially constant. All samples took around one day to gel, which is a value higher than expected. This time enlargement has to be attributed to the amount of ethanol employed during the process, since it hinders the hydrolysis and reduces the catalyst performance by a dilution effect. It has to be noted that this effect has no severe implications on the structure of samples if the solvent evacuation is extremely slow during the drying procedure. Samples S1, S2 and S2M have been extracted from Table 1 as three distinct cases, illustrating the variety of magnetic properties as a consequence of pH and aging time variations.

The thermal evolution of the samples was previously studied by thermogravimetry, to optimize the heat treatment route. Fig. 1 shows the curves registered for samples S2 and S2M in derivative mode (DTG). Total weight loss (up to 700 °C) of S2 and S2M samples was 68% and 54%, respectively, but it is noticeable that the main weight loss occurs before 300 °C. Sample S2 DTG shows a pronounced peak around 100 °C, due to desorption of water and ethanol physically retained at the pore gel surface, leading to a 40% weight loss. A second peak appears at 210 °C with a shoulder at 260 °C (24% weight loss), typically assigned to carbonization of remaining organic compounds, complete decomposition of NO_3^- ions from the starting salt and hydrogen-bonded formamide at the xero-

Table 1
Main parameters of the sol–gel processing for a sample set varying pH and aging time

Sample	Gelation		Aging		Drying		pH	Ms (emu/g)
	Time (days)	T (°C)	Time (days)	T (°C)	Time (days)	T (°C)		
1	1	50	50	50	5	50	0.74	0.09
2	1	50	20	50	5	50	0.74	0.034
3 (S1)	1	50	7	50	5	50	0.74	0.20
4	1	50	50	50	5	50	1	0.50
5	1	50	20	50	5	50	1	1.23
6	1	50	7	50	5	50	1	0.14
7 (S2M)	1	50	120	50	5	50	2	0.50
8	1	50	20	50	5	50	2	4.59
9	1	50	10	50	5	50	2	6.45
10 (S2)	1	50	7	50	5	50	2	8.03

T stands for temperature and M_S for saturation magnetization at 300 K.

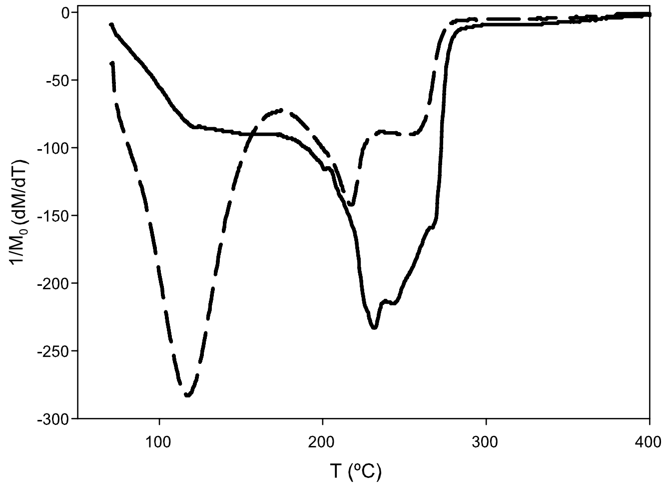

Fig. 1. DTG of S2 (dotted line) and S2M (full line) samples, illustrating the structural influence of post-aging in the studied composites.

gel surface [18]. A further weight loss takes place beyond 550 °C, which is typically assigned to the removal of water coming from additional polycondensation and dehydroxylation of iron oxyhydroxides [19].

A similar profile was obtained for sample S1. In contrast, DTG of S2M sample reveals some differences related to maturing effect in the nanocomposites. This effect leads to a 20% reduction of the total weight loss, mainly due to the elimination of most water and alcohol excess, as revealed the less significant DTG first peak (15% weight loss). Nevertheless, the increase of the weight loss above 200 °C (36%) indicates that additional surface reactions are promoted during this step which, as described later, will influence the Fe_2O_3 particles formation. It is very noticeable that the later peak grows at the expense of the first one. The second DTG peak is referred to the process of oxyhydroxides formation from adsorbed water and other hydroxilated species present inside the gel [20].

When experiments are carried out in an oxygen atmosphere, no remarkable differences are noticed in the curves, except for a better resolution of 210 and 260 °C peaks. However, nanocomposites appearance, once treated at 700 °C, is significantly different depending on the atmosphere: in oxygen flow, clean reddish pieces of glassy gel are obtained whereas nitrogen flow induces a progressive darkening from core to surface of the samples. This observation could be related to the absence of oxygen in the surface surroundings, although it is generated inside the pores from oxygenated organic compounds decomposition. Other authors have pointed out that organic residues promote the conversion to maghemite trough a magnetite intermediate transition [21,22], but in those cases, the highly probable formation of iron oxyhydroxides as precursors of final oxides [23] was not taken into account as well as no direct measurements indicating the existence of magnetite were provided. In agreement with the results from DTG experiments, elimination of the solvents and organic residues trapped in the gel network and promotion of maghemite particles formation, were accomplished by heat treating the samples under N_2 stream at 0.5 °C/min up to 700 °C, following a multi-ramp path with steps at 100 °C (16 h), 180 °C (6 h), 300 °C (3 h) and 700 °C (3 h). It is noteworthy to remark that, in most of the cases, an inert atmosphere, e.g. nitrogen, is needed to observe the transformation to γ-Fe_2O_3 phase [24], while oxygen favors the appearance of α-Fe_2O_3. Furthermore, the presence of water vapor either generated in the sample surroundings during water evacuation from the xerogel pores or contained within the employed gas flow, also enhances the formation of α-Fe_2O_3, as demonstrated in dedicated experiments with water saturated gas flows [25]. Finally, the temperature was reduced at 0.5 °C/min down to room temperature, and iron oxide doped silica xerogels resulted, with physical and mechanical properties dependent of processing conditions.

Fig. 2 shows the XRD patterns corresponding to the three samples studied obtained at room temperature. At low diffraction angles, we may observe the typical broad diffraction halo due to the amorphous silica matrix. At higher angles, several diffraction peaks appear which can be assigned to both γ-Fe_2O_3 (○) and α-Fe_2O_3 (■) phases, as indicated on these profiles. It should be noticed that peaks are more intense for samples prepared at $pH = 2$, S2 sample showing the best γ phase conversion, as revealed by the large 36° peak, assigned to maghemite.

As a general trend, a slight broadening of the Bragg peaks full-width-at-half-maximum (FWHM) is observed with the decreasing in processing pH, pointing out the expected particle size increases from S1 to S2M or S2 samples. However, the most noticeable effect due to additional aging is the presence of α-Fe_2O_3 phase reflections in a larger extent in the S2M pattern than in the S2 one. So, whereas the S2 sample contains mainly γ-Fe_2O_3 phase, sample S2M includes a mixture of both phases.

This trend is confirmed by information derived from TEM micrographs (Fig. 3). As shown in Fig. 4, histograms corresponding to S2M and S2 comprise a broader size range than that obtained for sample S1, with a mean particle size of 3 nm, as opposite to 5 nm for the former ones. In fact, the intensity decrease observed in the most characteristic peaks of S1 diffraction pattern is surely related with a higher number of small particles. S2 histogram illustrates a broad particle size distribution with a large amount of smaller nanoparticles. Regarding the particles shape, TEM micrographs show quasi-spherical particles in all the samples.

On the other hand, Fig. 5 shows ^{57}Fe Mössbauer spectra corresponding to the three studied samples. The spectra clearly shows two main contributions as arising from components with different magnetic behaviors; one sextet corresponding to ferrimagnetic maghemite and one doublet due to the superparamagnetic behavior exhibited by the smallest particles, diminishing the doublet/sextet ratio from S1 to S2. The fitting of the spectra has been performed using the NORMOS program, developed by Brand et al.

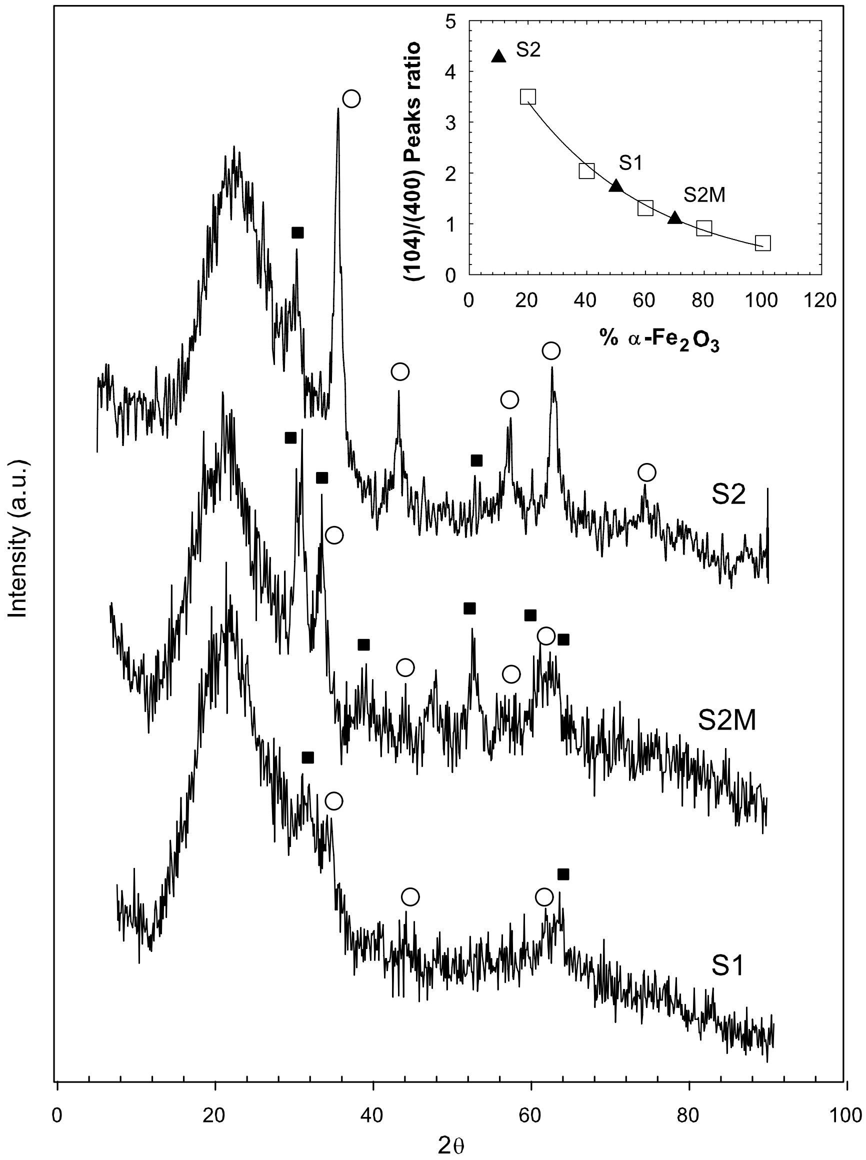

Fig. 2. XRD spectra of samples S1, S2M and S2. The most characteristic peaks of each iron oxide phase are marked with (○) for the maghemite reflections and with (■) for the hematite ones. The inset shows the relationship between two selected peaks ratio in commercial maghemite/hematite mixtures (□) and hematite percentage. Each sample (▲) is located along the line that best fits this relationship, and an estimation of their hematite content is made.

[26]. This allows a simultaneous fit of crystalline spectra with the possible addition of a distribution of hyperfine fields B_{HF}. As it can be observed in the spectra, the magnetic component is the result of contributions from different magnetically non-equivalent Fe atoms presented in the same phase. This fact can be understood if we take into account the microstructure of the sample. There is not a homogeneous size for the nanoparticles and, besides, the surface and bulk atoms present different chemical surroundings. As the Mössbauer spectroscopy is a local technique, these differences will be reflected in the subspectrum hindering the fitting of the later by two well differenced sextets. For this reason, we have chosen a distribution of hyperfine fields to fit the magnetic component, whose results are presented at the right hand of Mössbauer spectra. The corresponding hyperfine parameters of samples and those of pure oxides are summarized in Table 2, for comparison. All parameters were referred to α-Fe at room temperature. The isomeric shift and quadrupolar shifting values extracted from Mössbauer spectra fall within the typical range attributed to Fe^{3+} ions and reveals its high spin state. Furthermore, the calculations of doublet/sextet area ratios let us valuate the percentage of those phases in superparamagnetic state corresponding to each sample: 73.4% (S1), 60.0% (S2M) and 16.8% (S2).

Finally, Fig. 6 shows the magnetization curves of the samples at 300 K. At this temperature, they are non-hysteretic, as expected for samples which should contain nanoparticles both above and below the superparamagnetic (SPM) limit, but in the unblocked regime. There is not a

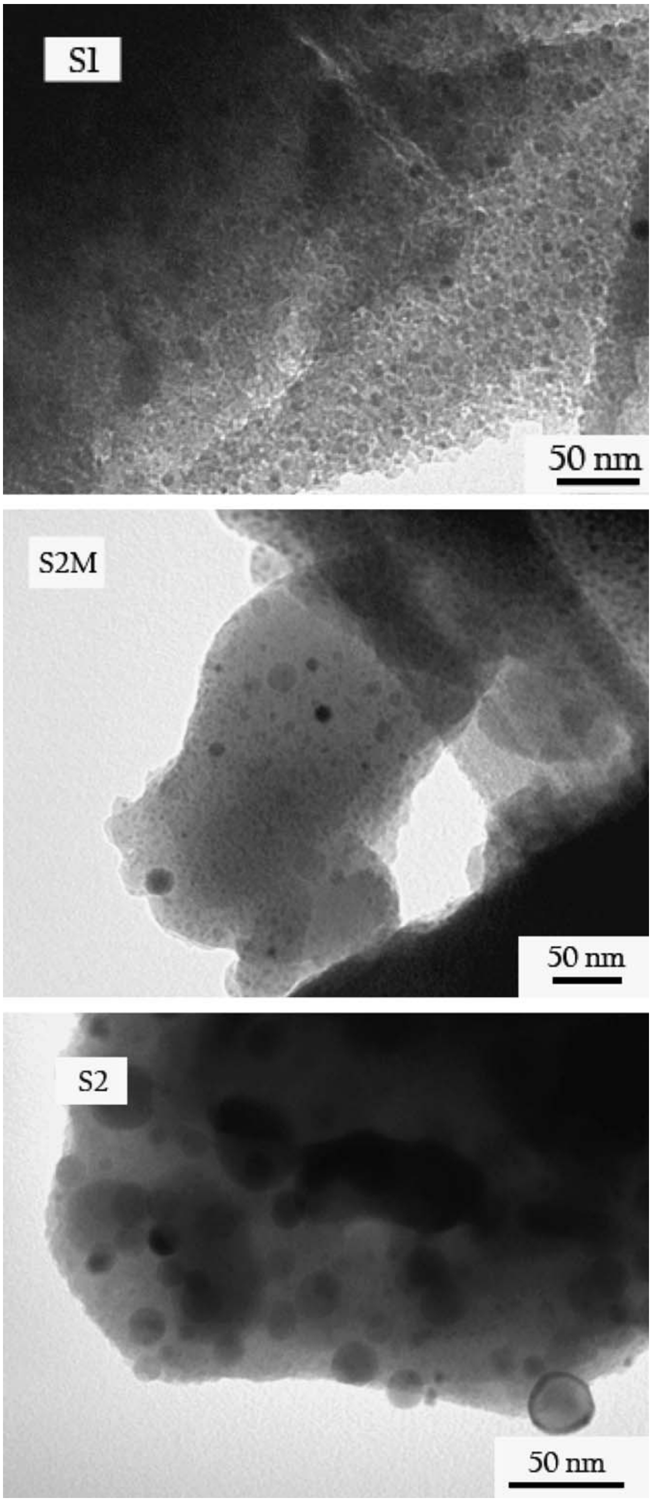

Fig. 3. TEM micrographs of the three samples under study, showing the size and morphology of iron oxide nanoparticles.

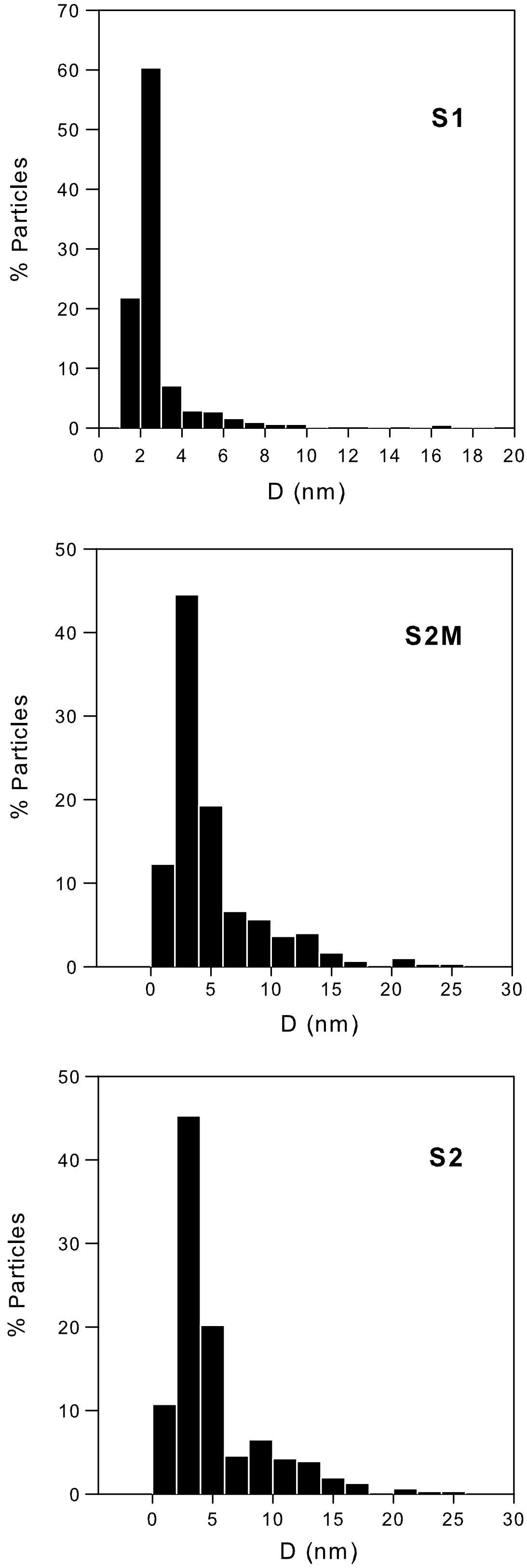

Fig. 4. Size distribution histograms obtained from TEM micrographs.

simple relationship to describe the magnetic behavior of the samples, due to the complex Fe_2O_3 phase composition. In principle, we may have γ-Fe_2O_3 particles both above and below the SPM limit, as mentioned before, but also antiferromagnetic α-Fe_2O_3 particles. At first glance, magnetization decreases with aging time and pH which, as we shall discuss later, may be derived from both particle size and the phase of the formed iron oxide.

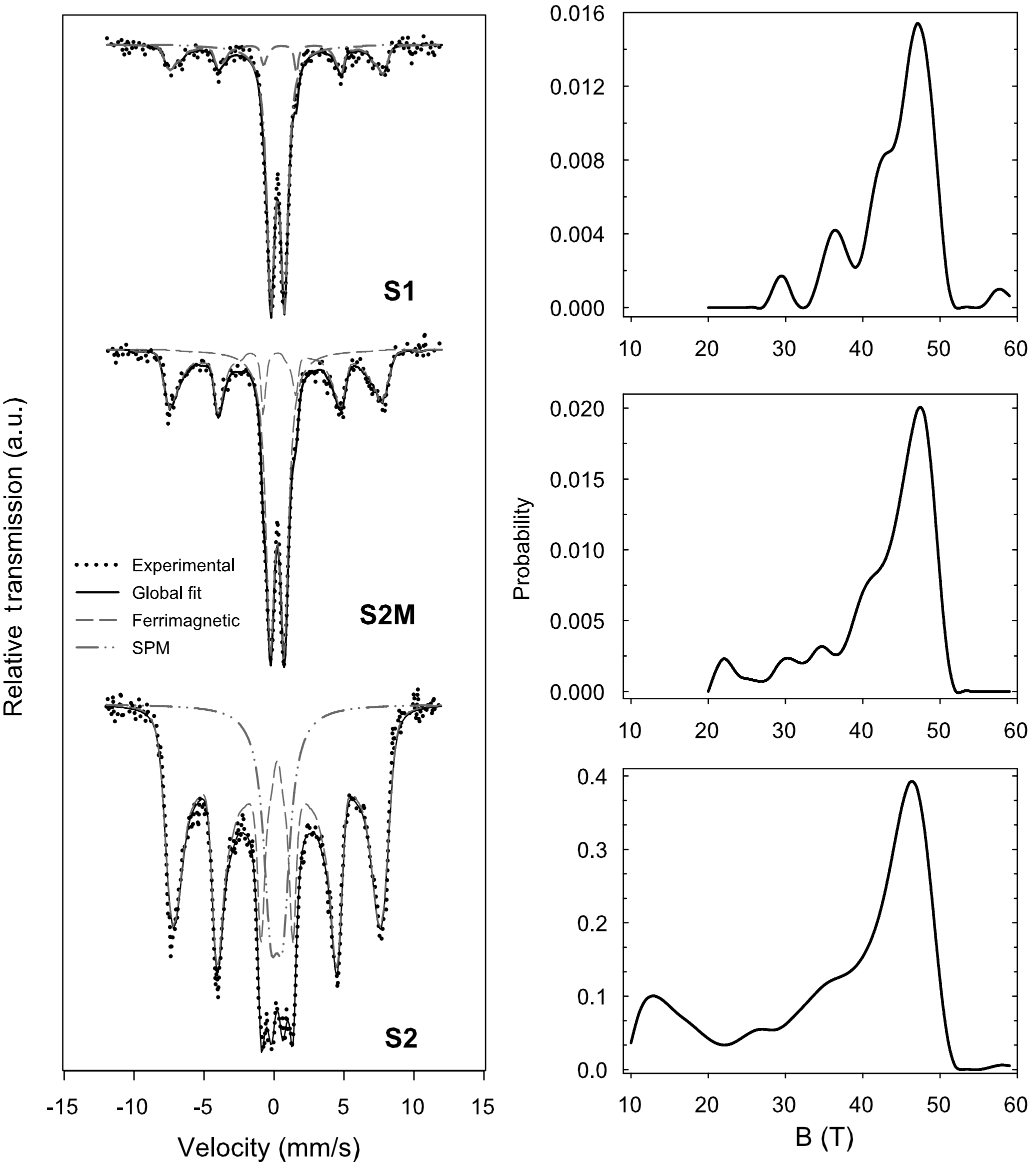

Fig. 5. Mössbauer spectra of samples S1, S2M and S2 at room temperature and the corresponding hyperfine field distributions.

Table 2

Mössbauer hyperfine parameters of magnetic phases in S1, S2M, S2, isolated maghemite and hematite: isomer shift (δ), quadrupolar shifting (2ε), quadrupolar splitting (Δ), Hyperfine field (B), FWHM and doublet/sextet ratio (d/s)

Sample		δ (mm/s)	Δ (mm/s)	2ε (mm/s)	B (T)	FWHM	d/s
S1	fM	0.34(1)	−0.23(1)		44.3(8)		2.76
	SPM	0.33(1)		0.96(1)		0.65(1)	
S2M	fM	0.37(1)	−0.15(1)		42.7(4)		1.50
	SPM	0.33(1)		1.00(1)		0.74(1)	
S2	fM	0.51(1)	0.25(1)		37.1(2)		0.20
	SPM	0.33(1)		0.80(1)			
γ-Fe_2O_3 [38]		0.22	0.08		50.2		–
		0.37	0.02		50.5		
α-Fe_2O_3 [39]		0.38	−0.21		52.1		–

4. Discussion

Many efforts have been addressed to avoid the appearance of hematite during the treatment of gel hosted iron-oxide particles [27], showing very broad transition temperatures covering from 600 to about 900 °C even for similar sample preparation. Such studies illustrate that, despite of the phase isolation attempts, the transformation strongly

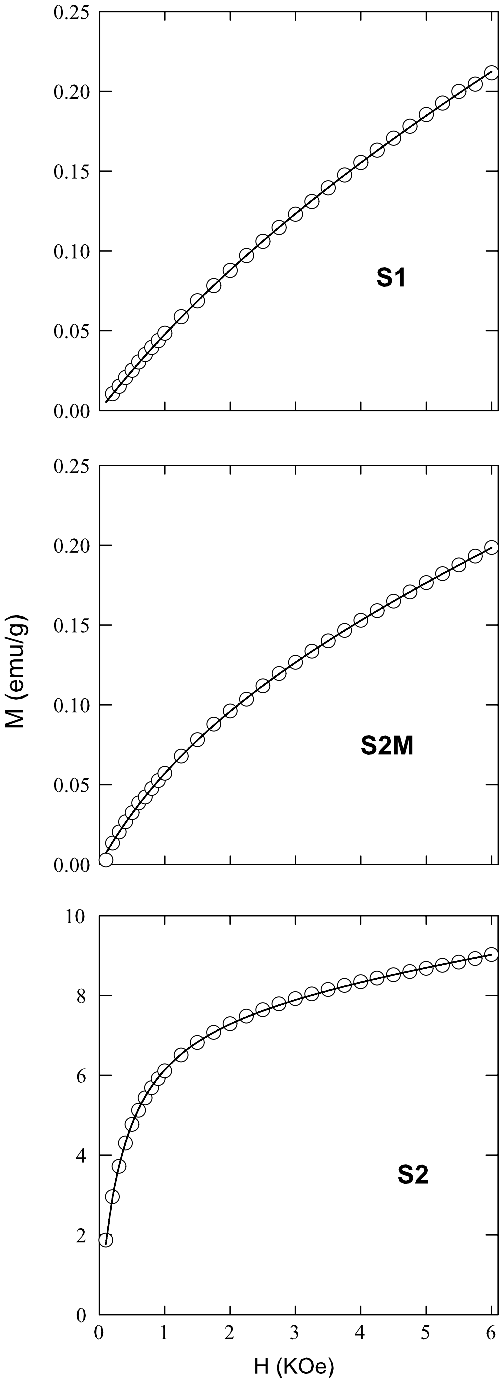

Fig. 6. Magnetization curves for S1, S2M and S2 registered at 300 K showing the experimental data (○) and curve fit (–).

depends on the sample processing, and in all cases it has been found the eventual occurrence of hematite.

Thermogravimetric results reveal that the samples processing preserve a significant amount of residues to remove, which are sensitive for interaction with iron oxide precursors. In fact, the evolution of DTG peaks when additional aging takes place, indicates a major contribution of the second peak in 200–300 °C range to the total weight loss. Both S2 and S2M gels exhibit the loss from nitrates decomposition just at the starting of the second DTG peak. As we shall show in a future paper, the decrease in the ratio of the first peak area to the second one progressively occurs as iron content becomes higher, since hydroxyl groups from solvents and silanol groups at the gel surface are involved in the oxyhydroxides formation. Solvent volume employed in our samples is enough to dissolve 15 wt% iron, ensuring a complete transformation. Fig. 1 demonstrates that aging time in samples favors the conversion to oxyhydroxides, as well as allows the sol–gel reactions to continue beyond drying stage, establishing a competition between them that will mark the phase and the size of nanoparticles inside. The fact that effective weight loses only appears up to 300 °C probably indicates that, for increasing temperatures, the main processes are phase changes in the iron oxide nanoparticles and, in a lower extension, particle growth [28].

A general analysis of diffraction patterns presented in Fig. 2 reveals that, firstly, not all characteristic peaks of iron oxide phases are clearly shown and, secondly, peak intensities and widths differ from those expected for a bulk sample. Other authors have pointed out that the presence of additional phases to maghemite is observed when iron contents exceed 23 wt% [29]; in our samples, the iron content is, however, lower than this level and both maghemite and hematite phases could be clearly identified from diffraction patterns, depending on the Fe/Si ratio and processing conditions. It should be apparent from the S1 diffraction pattern an intensity decrease in most characteristic peaks as a consequence of the higher number of smaller particles. The size reduction apparently produced by the pH decreasing can be due to the competition between particle growing process and both the structural relaxation and further polycondensation of the gel network. Generally, at a given temperature, formamide concentration and composition of TEOS/Ethanol/Water system, the higher the pH the larger the gel pores [30]. In more acidic conditions (like sample S1), the hydrolysis reaction is favored, generating a weakly branched system, which will produce the solid gel. These conditions accelerate the first stage cross-linking of silica network, leaving smaller holes for particles to grow in.

In accordance with TEM and XRD observations, the amount of nanoparticles in superparamagnetic state grows from S2 to S1 as pH is decreasing, as indicated by the interpretation of Mössbauer spectra. As compared with isolated oxides, the nanocomposites hyperfine field values from Mössbauer data fits are generally lower. This can be interpreted from the synergy between the increasing numbers of atoms at particles' surface as well as the related surface spin canting. To our knowledge, nanoparticles are not chemically bonded to matrix, so dipolar interactions are more likely than superexchange to reduce hyperfine field.

From S1 to S2, the emerging of a ferrimagnetic sextet due to the presence of maghemite particles is observed, and its area increases at the expense of the central doublet. This contribution to the spectra takes place while the central doublet is gradually broadening. The anisotropy energy, supposing a single domain uniaxial particle system, is given by:

$$E_a = KV \sin^2 \theta, \tag{1}$$

where K is the anisotropy constant, V the volume and θ the angle between the magnetization and the easy axis of magnetization. Anisotropy expression of maghemite/hematite is rather more complex than that expressed in Eq. (1), but it is worth to make that simplification for the following discussion. From S2 to S1, V is decreasing down to a critical value which allows the thermal fluctuations to continuously reverse the spin orientation. In that sense, S1 contains a larger fraction of superparamagnetic particles with a modest ferrimagnetic contribution from the rest of maghemite particles. On the other hand, S2 exhibits a magnetically split sextet coupled with a more or less wide doublet. The S2 profile is rather different from those of S1 and S2M, with an asymmetrically broadening of lines, probably due to the enhanced interactions between nanoparticles. TEM images of S2M and S2 are very similar and from them, almost the same particle distribution is obtained, but their magnetic behavior is quite different. The explanation of this fact must be found in the iron oxide phase obtained after high temperature treatments. The vast majority of the iron atoms present within the sample belongs to the ferrimagnetic larger particles because they posses a higher volume than the smaller ones, nevertheless there are a greater number of α-Fe_2O_3 particles compared to the γ-Fe_2O_3 ones. It is possible to make an estimation of the weighed contribution of each type of particles to sample magnetization, by means of the diameter/volume relationship and Mössbauer data. An estimation of the superparamagnetic limit can be obtained if the SPM phase percentage, calculated from the relative area of doublet to sextet signals in the Mössbauer spectrum of sample S2, is compared with its volume distribution function, deduced from particle size distribution histogram in Fig. 4. For sample S2, SPM phase composition is estimated as 16.8% and this percentage corresponds to the volume of particles with diameter below 10 nm. This value is not far from the estimations made by other authors for similar systems [31].

Magnetization curves have been fitted considering the different phases contributions: (i) for maghemite nanoparticles above the SPM limit, a simple Fröhlich relationship has been considered; (ii) for γ-Fe_2O_3 nanoparticles below the SPM limit, the usual Langevin function was taken into account and (iii) for hematite nanoparticles, we have considering, as shown by Nèel [32–34], that they may have a net magnetic moment, due to the non-exact compensation of the two magnetic sublattices, i.e. the imbalance in the number of 'up and down' spins in its structure. According to Nèel [35], the uncompensated moment of AFM particles is given by

$$\mu_p = \mu_A N^{\alpha}, \tag{2}$$

where μ_A is the atomic moment and N is the number of magnetic atoms per particle. In the case of hematite, α has been proposed to be 1/3, due to its structure, composed of alternating compensated planes with incomplete top and bottom planes (i.e. where randomness in the distribution of magnetic ions occurs only on the particles surface).

Thus, the contribution to magnetization from these AFM particles is considered as:

$$M_{AFM} = N_{p,AFM} \cdot \mu_{p,avg}, \tag{3}$$

where $N_{p,AFM}$ is the number of hematite particles and $\mu_{p,avg}$ is their average magnetic moment, i.e. an average size for these kind of particles is considered here. This average size is taken from the TEM measurements in Figs. 3 and 4.

Considering the magnetization coming from all the phases and their different behavior with applied magnetic field, the experimental curves were fitted to the following relationship:

$$M = x_{AFM} M_{AFM} + x_{fM} M_{fM} + x_{SPM} M_{SPM}, \tag{4}$$

where x_{AFM}, x_{fM} and x_{SPM} are, respectively, the estimated fractions of α-Fe_2O_3, γ-Fe_2O_3 in particles above the SPM limit and those below this limit. As previously mentioned, for the second contribution, a Fröhlich [36,37] (non-hysteretic) relationship has been considered. Thus, the magnetization from the bigger maghemite particles is taken as

$$M_{fM} = \frac{\alpha H}{1 + \beta H}, \tag{5}$$

where α/β gives the saturation magnetization for this phase.

On the other hand, for the maghemite particles below the SPM limit, the M_{SPM} is deduced from the usual Langevin function

$$M_{SPM} = N_{SPM}\mu_{SPM}\left[\coth\left(\frac{\mu_0 \mu_{SPM} H}{k_B T}\right) - \frac{k_B T}{\mu_0 \mu_{SPM} H}\right], \tag{6}$$

where N_{SPM} is the number of SPM particles with average magnetic moment μ_{SPM}, also taken from the size distribution in Fig. 4.

Table 3 summarizes all the results obtained in the fittings of magnetization curves, comparing them with those obtained from XRD measurements. Magnetization of sample S1 corresponds to a set of very small particles with an almost equal fraction of hematite and maghemite phases. This result is compatible both with XRD measurements (Fig. 2) and size distribution histogram deduced from TEM observations (Fig. 4). In the cases of samples S2 and S2M, interpretation is more complex. For sample S2, a 73% of ferromagnetic phase (γ-Fe_2O_3 particles above the SPM limit) is estimated. For this result to be in agreement with the size distribution of Fig. 4, the SPM limit must be set around 13 nm and it has to be considered that there are not hematite particles in this high size range. The amount of hematite and maghemite particles with sizes below this limit is almost identical. Although most of the particles are in the blocked state, the magnetization curve is still essentially anhysteretic, i.e. blocked particles must have a low coercivity, as a consequence of γ-Fe_2O_3 cubic

Table 3
Estimated composition of samples deduced from XRD and from magnetization curve fittings to Eq. (4)

Sample	Composition estimated from XRD		Composition estimated from magnetization curve fittings		
	α-Fe_2O_3 (%)	γ-Fe_2O_3 (%)	α-Fe_2O_3 (%)	SPM γ-Fe_2O_3 (%)	fM γ-Fe_2O_3 (%)
S1	50	50	54	45	1
S2M	70	30	65	33	2
S2	10	90	12	15	73

structure, spherical shape of particles and random orientation of their magnetic moments that would lower magnetic anisotropy. Additionally, the fact that bigger particles may be multidomain cannot be ignored.

On the contrary, for sample S2M, with a size distribution diagram similar to that of sample S2, the majority phase must be hematite, even more in the high size range, to accomplish the magnetization curve. This fact can be also observed in the XRD pattern of Fig. 2, where hematite reflections are more noticeable than maghemite ones in this sample. Values of relative hematite and maghemite composition, deduced from the comparisons of XRD patterns with those of several mixtures of commercial hematite and maghemite powders, are also in agreement with these values deduced from the magnetization fits. The estimated value of the SPM limit here is larger than the one obtained in a similar way from Mössbauer spectra, but this is an expected result if one considers the different experimental time in both techniques.

5. Conclusions

Several Fe_2O_3/SiO_2 nanocomposites have been prepared by sol–gel process, using iron (III) nitrate as nanoparticles precursor. After drying and aging, doped xerogels were heat treated up to 700 °C. Samples were characterized by XRD, TEM, TGA, Mössbauer spectroscopy and Faraday magnetometry. It was found that modifying aging and pH conditions used in the synthesis of Fe_2O_3/silica nanocomposites, it is possible to tune up the size and phase of embedded nanoparticles, thus determining their magnetic properties. Although all the samples exhibit a mixture of α and γ iron oxide phases, it has been shown that higher pH conditions and shorter aging time, leads to a higher maghemite conversion efficiency, with a larger nanoparticle size. Thermogravimetry experiments reveal the influence of aging time on the resulting phases, by modifying the conversion route from the iron nitrate precursor to the final oxide.

The most significant features from XRD patterns are a peak broadening trend as pH decreases (due to the smaller size of the particles, confirmed by TEM) and the increase of reflections from α iron oxide phase (as a result of the aging time).

The nanoparticles size and iron oxide phase mixture govern the magnetic behavior revealed by Mössbauer spectroscopy and magnetization measurements. By fitting Mössbauer and magnetization curves, taking into account XRD and size distribution histograms from TEM, estimations of 10 nm (Mössbauer) and 13 nm (magnetometry) for the SPM limit of γ-Fe_2O_3 nanoparticles have resulted. It can be concluded that processing conditions of S2 sample leads to a better ferrimagnetic nanoparticles conversion yield. Yet, due to their small particle size and matrix nature, these composites still possess an acceptable transparency which, combined with the observed magnetic properties, make them suitable to be used in magneto-optical devices.

Acknowledgements

These investigations have been supported by the Spanish MCyT/FEDER under projects MAT2002-02179 and MAT2002-04087-C02-C01. The authors would like to gratefully thank to J. González, J. M. González-Leal and R. Litrán for the technical support and fruitful discussions.

References

[1] A. Bourlinos, A. Simopoulos, D. Petridis, H. Okumura, G. Hadjipanayis, Adv. Mater. 13 (2001) 289.
[2] D. Jamon, S. Robert, F. Donatini, J.J. Rousseau, C. Bovier, H. Roux, J. Serrughetti, V. Cabuil, D. Zins, IEEE Trans. Magn. 37 (2001) 3803.
[3] P. Mazzoldi, G.W. Arnold, G. Battaglin, F. Gonella, R.F. Haglund, J. Non-Linear Opt. Phys. Mater. 5 (1996) 285.
[4] P. Chakraborty, J. Mater. Sci. 33 (1998) 2235.
[5] R.D. Shull, J.J. Ritter, A.J. Shapiro, L.J. Swartzendruber, L.H. Bennett, J. Appl. Phys. 67 (1990) 4490.
[6] E. Tronc, D. Fiorani, M. Nogues, A.M. Testa, F. Lucari, F. Orazio, J.M. Greneche, W. Wernsdorfer, N. Galvez, C. Chaneac, J. Magn. Magn. Mater. 262 (2003) 6.
[7] C. Caizer, C. Savii, M. Popovici, Mater. Sci. Eng. B 97 (2003) 129.
[8] C. Caizer, Phys. B: Cond. Matter. 327 (2003) 27.
[9] F. Bentivegna, M. Nyvlt, J. Ferre, J.P. Jamet, A. Brun, S. Visnovsky, R. Urban, J. Appl. Phys. 85 (1999) 2270.
[10] R.F. Ziolo, E.P. Giannelis, B.A. Weinstein, M.P. O'Horo, B.N. Ganguly, V. Mehrotra, M.W. Russel, R. Huffman, Science 257 (1992) 219.
[11] F. Bentivegna, J. Ferre, M. Nyvlt, J.P. Jamet, D. Imhoff, M. Canva, A. Brun, P. Veillet, S. Visnovsky, F. Chaput, J.P. Boilot, J. Appl. Phys. 83 (1998) 7776.
[12] G. Rosa, H. Guerrero, D. Levy, A. Alvarez-Herrero, J. Appl. Phys. 97 (2005) 064314.
[13] T.W. Cease, J.G. Driggans, IEEE Trans. Power Deliver 6 (1991) 1374.
[14] H. Katsukawa, H. Ishikawa, H. Okajima, T.W. Cease, IEEE Trans. Power Deliver 11 (1996) 702.
[15] D. Ortega, PhD Thesis, Universidad de Cadiz, 2006.
[16] A.E. Gash, T.M. Tillotson, J.H. Satcher, L.W. Hrubesh, R.L. Simphon, Chem. Mater. 13 (2001) 999.
[17] C.M. Flynn Jr., Chem. Rev. 84 (1984) 34.

[18] E. Blanco, M. Ramirez-del-Solar, N. de la Rosa-Fox, L. Esquivias, Mater. Lett. 22 (1995) 265.
[19] L. Li, G. Li, R.L. Smith, H. Inomata, Chem. Mater. 12 (2000) 3705.
[20] S. Ponce-Castañeda, J.R. Martínez, F. Ruiz, S. Palomares-Sánchez, O. Domínguez, J. Sol–Gel. Sci. Tech. 25 (2002) 29.
[21] T. Gonzalez-Carreno, M.P. Morales, M. Gracia, C.J. Serna, Mater. Lett. 18 (1993) 151.
[22] F. del Monte, M.P. Morales, D. Levy, A. Fernandez, M. Ocana, A. Roig, E. Molins, K. O'Grady, C.J. Serna, Langmuir 13 (1997) 3627.
[23] S. Ponce-Castañeda, J.R. Martínez, S. Palomares-Sánchez, F. Ruiz, O. Ayala-Valenzuela, J.A. Matutes-Aquino, J. Sol–Gel. Sci. Tech. 27 (2003) 247.
[24] K. Woo, H.J. Lee, J.P. Ahn, Y.S. Park, Adv.Mater. 15 (2003) 1761.
[25] G.S. Chopra, C. Real, M.D. Alcala, L.A. Perez-Maqueda, J. Subrt, J.M. Criado, Chem. Mater. 11 (1999) 1128.
[26] R.A. Brand, J. Lauer, D.M. Herlach, J. Phys. F: Metal Phys. (1983) 675.
[27] I.K. Battisha, H.H. Afify, I.M. Hamada, J. Magn. Magn. Mater. 292 (2005) 440.
[28] C. Cannas, G. Concas, A. Musinu, G. Piccaluga, G. Spano, Z. Naturforsch., A: Phys. Sci. 54A (1999) 513.
[29] P. Ayyub, M. Multani, M. Barma, V.R. Palkar, R. Vijayaraghavan, J. Phys. C: Solid State Phys. (1988) 2229.
[30] C.J. Brinker, G.W. Scherer, Sol gel science. The physics and chemistry of sol–gel processing, Academic Press Inc., 1990.
[31] J.L. Dormann, D. Fiorani, E. Tronc, Magnetic relaxation in fine-particle system, John Wiley, New York, 1997.
[32] L. Nèel, C. R. l'Academie. Sci. 252 (1961) 4075.
[33] L. Nèel, C. R. l'Academie. Sci. 253 (1961) 9.
[34] L. Nèel, C. R. l'Academie. Sci. 253 (1961) 1286.
[35] L. Néel, Low Temperature Physics, Gordon & Breach, London, 1962.
[36] R.D. Zysler, D. Fiorani, A.M. Testa, J. Magn. Magn. Mater. 224 (2001) 5.
[37] D.C. Jiles, Introduction to Magnetism and Magnetic Materials, Chapman and Hall Publishers, London and New York, 1998.
[38] H. Annersten, S.S. Hafner, Z. Kristallogr. 137 (1973) 321.
[39] F.V.d. Woude, Phys. Stat. Sol. 17 (1966) 417.